

Hybrid Small-Signal Modeling of GaN HEMT Enhanced by the Integration of SVD and RIME Optimization

Jincan ZHANG, Kexin WANG, Jinchan WANG, Haobo WEI,
Jingyu CHANG, Jiahao YAO, Liwen ZHANG

College of Information Engineering, Henan University of Science and Technology, Luoyang 471023, China

zjc850126@163.com

Submitted June 26, 2025 / Accepted October 1, 2025 / Online first October 24, 2025

Abstract. For the 20-element small-signal model of GaN HEMT, a combination of the Singular Value Decomposition (SVD) algorithm and the frost ice optimization algorithm is proposed in this paper to extract and optimize the intrinsic parameters of the small-signal model. When the traditional algorithm is employed for parameter extraction, issues of low extraction accuracy and efficiency are encountered. By introducing an optimization algorithm for parameter extraction, the accuracy and efficiency of the process are enhanced. However, previous studies have focused on improving the optimization algorithm to optimize the eigenparameters of GaN HEMT without taking into account the correlation among the parameters within the model. In this study, the SVD algorithm is utilized to process the real and imaginary parts of the intrinsic model Y-parameters, thereby strengthening the correlation between the intrinsic parameters. Subsequently, the new intrinsic model Y-parameters and the RIME algorithm are employed to extract the intrinsic parameters. The experimental results demonstrate that the combination of the SVD algorithm and the frost ice optimization algorithm breaks the isolation between the eigenparameters, improves the parameter correlation, and can accurately extract and optimize the eigenparameters of the small-signal model within the frequency range of 0.5–20.5 GHz.

Keywords

GaN HEMT, small-signal model, hybrid approach, Singular Value Decomposition (SVD) algorithm, Rime Optimization algorithm

1. Introduction

In recent years, the growth in demand for millimeter-wave high-power amplifiers has been fueled by the proliferation of wireless communication technologies such as 5G and SATCOM [1–4]. III-V semiconductors, especially GaN and InP, have been recognized as leading materials due to their high electron mobility, good lattice matching,

low energy consumption and simplified manufacturing processes. These properties make them widely used in high-frequency environments [5–7]. Among them, GaN stands out with its huge band gap, high electron saturation drift rate, strong thermal conductivity and relatively low dielectric constant, and has been made the focus of current research efforts [1, 3, 8]. GaN HEMTs can be operated in extreme conditions, such as high temperatures, high pressures, and radiation-exposed environments. They are characterized by distinctive advantages in high-frequency, high-power scenarios and have emerged as highly promising candidates for such applications [9–12]. The behavior of devices under small-signal conditions is elucidated by small-signal circuit models, which are the cornerstone of device and circuit design. To achieve effective circuit design, accurate modelling techniques are essential to maximize design efficiency [11, 13, 14]. Therefore, there is an urgent need for an in-depth study of small-signal modelling of GaN HEMTs.

At the beginning of the 21st century, a 14-element small-signal model of GaN HEMTs was constructed by Chigaeva et al. [15], [16] through the measurement of S-parameters of cold field-effect transistors and direct parameter extraction at high gate voltages. However, this method was unable to obtain reliable values for parasitic inductance. Ahmad proposed the use of Support Vector Regression (SVR) to analyze the small-signal behavior of GaN [17] and employed a strategy to optimize the extracted parameters. Nevertheless, the entire process was complicated, and the efficiency of parameter extraction was not high. In recent years, the topology and parameter extraction methods for GaN HEMT small-signal models have been continuously developed and are gradually becoming mature [18]. Current methods for small-signal parameter extraction mainly include direct extraction techniques and extraction techniques based on optimization algorithms. A large number of papers have reported the use of optimization algorithms for parameter fitting, and this technique is promising as it is not only easy to implement but also yields excellent final results [19], [20]. Meanwhile, related research has previously been conducted by us, and relevant papers have been published [21], [22]. However, in those

study, attention was only given to improving the optimization algorithm when optimizing the intrinsic parameters of GaN high electron mobility transistors, while the correlation between the parameters within the model was not taken into account.

To address the aforementioned issues, in this paper, model parameters are extracted based on a 20-element small-signal parameter model of GaN HEMT using a hybrid method that combines direct extraction techniques and the Singular Value Decomposition (SVD) algorithm-Frost and Ice algorithm [23–27]. Parasitic parameters are extracted using direct extraction techniques, and then intrinsic parameters are extracted and optimized using a combination of the SVD algorithm and the Frost and Ice algorithm. The Frost and Ice optimization algorithm is a nature-inspired algorithm based on the formation of frost ice. It has the advantages of a simple principle, ease of implementation, and adaptability to multi-dimensional variables, and has been applied in various fields [28], [29]. However, when intrinsic parameters are directly extracted using only the Frost and Ice algorithm, the correlations between the intrinsic parameters cannot be explained, and the parameters are isolated from each other. Therefore, in this paper, further research is conducted by introducing the SVD algorithm, which is an important algorithm for decomposing and reconstructing data to extract the intrinsic features of the data [30–32]. The algorithm first processes the real and imaginary parts of the Y-parameters of the GaN HEMT intrinsic model and then extracts the parameters using the new intrinsic model Y-parameters and the Rime Optimization (RIME) algorithm [33–35]. From the experimental results, it can be observed that the combination of the SVD algorithm and the Frost and Ice algorithm, through the processing of the intrinsic model Y-parameters, breaks the isolation between the intrinsic parameters, enhances the correlation between each intrinsic parameter, and improves the accuracy and reliability of the parameter extraction for the small-signal model.

In this paper the SVD-RIME algorithm is utilized for intrinsic parameter extraction and optimization of the small signal model. The structure of this paper is organized as follows: The second section introduces the equivalent circuit of the small-signal model for GaN HEMT. The third section presents the extraction of small-signal parameters for GaN HEMT, with a focus on using the SVD-RIME algorithm to extract the intrinsic parameters. The fourth section analyzes the results. The fifth section provides a summary of the paper.

2. Small-Signal Model

The equivalent circuit of the GaN HEMT small-signal model used in this paper is shown in Fig. 1. The equivalent circuit model is divided into an intrinsic circuit model and a parasitic circuit model, where the dashed box encloses the intrinsic circuit model and the area outside the dashed box represents the parasitic circuit model. The parasitic cir-

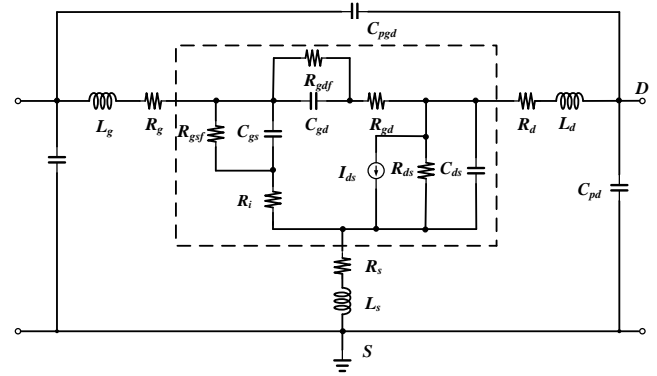


Fig. 1. GaN HEMT small-signal model equivalent circuit.

cuit model mainly consists of three types of parasitic components: parasitic capacitors (C_{pg} , C_{pd} , C_{pgd}), parasitic inductors (L_g , L_d , L_s), and parasitic resistors (R_g , R_d , R_s). The intrinsic circuit model is constructed based on the working mechanism of the GaN HEMT device, which alters the concentration of the 2DEG (Two-Dimensional Electron Gas) by adjusting the gate voltage, thereby changing the I_{ds} . The current source I_{ds} is represented as the current in the 2DEG channel. Among the intrinsic components, R_{gsf} and R_{gdf} are represented as the gate-source and gate-drain differential resistances, respectively. C_{gd} and C_{gs} are represented as the plate capacitors formed by the gate and the 2DEG channel charges. R_{ds} and R_i are represented as the resistances of the 2DEG channel, R_{gd} is represented as the resistance between the gate and the drain, and C_{ds} is represented as the geometric capacitance between the drain and the source.

3. Small-Signal Model Parameter Extraction

The parameter extraction of the small-signal model is mainly divided into two parts: the first part is the extraction of parasitic parameters, and the second part is the extraction of intrinsic parameters. In this paper, a method combining direct extraction with data processing-algorithm optimization is adopted for parameter extraction.

3.1 Parasitic Parameters Extraction

The extraction of parasitic parameters encompasses parasitic capacitors, inductors, and resistors. The parasitic capacitances C_{pg} , C_{pd} , and C_{pgd} are represented as the parasitic pad capacitances between the gate, drain, and gate-to-drain, respectively. The parasitic inductors L_g , L_d , and L_s are the lead parasitic inductances generated by the gate, drain, and source, respectively. The parasitic resistors R_g , R_d , and R_s are the parasitic resistances resulting from contact resistance effects.

1) Extraction of Parasitic Capacitances

A capacitive passive network is presented when the active device operates in the cut-off region. Under low-frequency conditions, parasitic resistances and parasitic

inductances can be neglected. Therefore, by adjusting the bias voltage to place the device in the cut-off state ($V_{GS} = -3$ V, $V_{DS} = 0$ V or $V_{GS} = -4$ V, $V_{DS} = 0$ V), the parasitic capacitors can be extracted under low-frequency conditions. The equations required for extracting the parasitic capacitors are shown in (1)–(5) [36]:

$$C_c = \alpha C_b, \quad (1)$$

$$\alpha = \frac{\text{Im}(Y_{a,22}) - \text{Im}(Y_{b,22})}{\text{Im}(Y_{b,12}) - \text{Im}(Y_{a,12})} - 1, \quad (2)$$

$$C_{pg} = \frac{1}{\omega} \text{Im}(Y_{a,11} + 2Y_{a,12}), \quad (3)$$

$$C_{pd} = \frac{1}{\omega} \text{Im}(Y_{a,11} + (1 + \alpha)Y_{a,12}), \quad (4)$$

$$\text{Im}(Y_{a,12}) = \text{Im}(Y_{a,21}) = -j\omega C_b \quad (5)$$

where $Y_{a,11}$, $Y_{a,12}$, $Y_{a,21}$, $Y_{a,22}$ are represented as the Y -parameters when the bias voltage is $V_{GS} = -3$ V and $V_{DS} = 0$ V, while $Y_{b,11}$, $Y_{b,12}$, $Y_{b,21}$, $Y_{b,22}$ are represented as the Y -parameters when the bias voltage is $V_{GS} = -4$ V and $V_{DS} = 0$ V. C_b is used to describe the injection layer resistance between the gate and the drain, C_c is a definition of coupling capacitance. α is a coefficient, and C_{pgd} is used to characterize the changes with different bias voltages. Since the value of C_{pgd} is very small, it can be neglected [37].

2) Extraction of Parasitic Inductances

After removing the influence of parasitic capacitors, the parasitic inductances are extracted under zero-bias conditions ($V_{GS} = 0$ V, $V_{DS} = 0$ V) [38], [39]. Under high-frequency conditions, the Z -parameters of the equivalent circuit model can be obtained as shown in (6)–(8):

$$Z_{zero,11} = R_g + R_s + \frac{1}{2}R_{ch} + \frac{1}{\omega^2 C_g^2 R_{dy}^2} + j\omega(L_g + L_s) - j\frac{1}{\omega C_g}, \quad (6)$$

$$Z_{zero,12} = Z_{zero,21} = R_s + \frac{1}{2}R_{ch} + j\omega L_s, \quad (7)$$

$$Z_{zero,22} = R_d + R_s + R_{ch} + j\omega(L_d + L_s). \quad (8)$$

The parasitic inductances can be directly obtained from the Z -parameters of the equivalent circuit model, and the extraction equations are shown in (9)–(11):

$$L_d = \frac{\text{Im}(Z_{zero,22} - Z_{zero,12})}{\omega}, \quad (9)$$

$$L_s = \frac{\text{Im}(Z_{zero,12})}{\omega}, \quad (10)$$

$$\omega \text{Im}(Z_{zero,11} - Z_{zero,12}) = \omega^2 L_g - \frac{1}{C_g} \quad (11)$$

Parameter	Value
C_{pds} (fF)	111.380
C_{pgs} (fF)	152.494
L_d (pH)	55.828
L_g (pH)	77.628
L_s (pH)	11.775
R_d (Ω)	6.202
R_g (Ω)	2.715
R_s (Ω)	2.950

Tab. 1. Extracted parasitic parameter values.

where $Z_{zero,11}$, $Z_{zero,12}$, $Z_{zero,21}$, $Z_{zero,22}$ are represented as the network parameters under zero-bias conditions. R_{ch} models channel conduction, R_{dy} captures frequency-dependent dissipation, and C_g characterizes the capacitive coupling of the gate.

3) Extraction of Parasitic Resistances

After removing the effects of parasitic capacitors and parasitic inductances, the parasitic resistances are extracted under reverse bias conditions ($V_{GS} = -2.5$ V, $V_{DS} = 0$ V) [4]. The extraction equations are shown in (12)–(14):

$$R_g = \text{Re}(Z_{11} - Z_{12}), \quad (12)$$

$$R_d = \text{Re}(Z_{22} - Z_{12}), \quad (13)$$

$$R_s = \text{Re}(Z_{12}) = \text{Re}(Z_{21}) \quad (14)$$

where Z_{11} , Z_{12} , Z_{21} , Z_{22} are represented as the network Z -parameters under reverse bias cut-off conditions.

The extraction results of the parasitic parameters are shown in Tab. 1. After extracting the parasitic parameters, de-embedding is performed to remove their interference. Then, the SVD-RIME algorithm is used to extract and optimize the intrinsic parameters.

3.2 SVD Algorithm

Owing to its proven efficacy in data decomposition and reconstruction, the SVD algorithm has been traditionally recognized as a highly efficient tool for data compression and dimensionality reduction. The core information in the data can be distilled by this algorithm while the essential features of the original dataset are preserved. In this paper, the SVD algorithm is utilized to process the intrinsic model Y -parameters, and a new intrinsic model Y -parameter extraction method is obtained.

3.2.1 Basic Principle of SVD Algorithm

The notion of aggregate set information is employed by SVD algorithms, which then describe and simplify the

structure of a data array using specific algebraic or set-criterion optimization techniques. The principle is as follows: if matrix $\mathbf{A} \in R^{m \times n}$, \mathbf{A} is a matrix of M rows and N columns with rank k , and $\text{Rank}(\mathbf{A}) = k$. Then there exists a set of orthogonal bases \mathbf{V} , $\mathbf{V} = [\mathbf{v}_1, \mathbf{v}_2, \dots, \mathbf{v}_k]$, \mathbf{A} matrices for which the transformations are still orthogonal bases, denoted as \mathbf{U} , $\mathbf{U} = [\mathbf{A}\mathbf{v}_1, \mathbf{A}\mathbf{v}_2, \dots, \mathbf{A}\mathbf{v}_k]$, and there exists Equation (15) when \mathbf{v} is an eigenvector of $\mathbf{A}^T\mathbf{A}$ [41], [42]:

$$(\mathbf{A}^T\mathbf{A})\mathbf{v}_i = \lambda\mathbf{v}_i \quad (15)$$

where λ is the eigenvalue of matrix $\mathbf{A}^T\mathbf{A}$. The mapped orthogonal basis \mathbf{U} is unitized as shown in (16), (17):

$$\|\mathbf{A}\mathbf{v}_i\|^2 = (\mathbf{A}\mathbf{v}_i)^T \times (\mathbf{A}\mathbf{v}_i) = \mathbf{v}_i^T \mathbf{A}^T \mathbf{A} \mathbf{v}_i = \lambda_i, \quad (16)$$

$$\mathbf{u}_i = \frac{\mathbf{A}\mathbf{v}_i}{\|\mathbf{A}\mathbf{v}_i\|} = \frac{1}{\sqrt{\lambda_i}} \mathbf{A}\mathbf{v}_i. \quad (17)$$

Equation (17) by simplifying and then using the matrix form can be expressed as (18):

$$\mathbf{A}\mathbf{V} = \mathbf{U}\mathbf{\Sigma} \quad (18)$$

where $\mathbf{V} = [\mathbf{v}_1, \mathbf{v}_2, \dots, \mathbf{v}_k] \in R^{n \times k}$, $\mathbf{\Sigma} = \text{diag}[\sigma_1, \sigma_2, \dots, \sigma_k]$, $\mathbf{U} = [\mathbf{u}_1, \mathbf{u}_2, \dots, \mathbf{u}_k] \in R^{m \times k}$, $\sigma_i^2 = \lambda_i$. Simultaneous right-multiplication of both sides of (18) by \mathbf{V}^T yields the singular value decomposition of matrix \mathbf{A} as shown in (19).

$$\mathbf{A} = \mathbf{U}\mathbf{\Sigma}\mathbf{V}^T = (\mathbf{u}_1, \mathbf{u}_2, \dots, \mathbf{u}_k) \begin{pmatrix} \sigma_1 & & & \\ & \sigma_2 & & \\ & & \ddots & \\ & & & \sigma_k \end{pmatrix} \begin{pmatrix} \mathbf{v}_1^T \\ \mathbf{v}_2^T \\ \vdots \\ \mathbf{v}_k^T \end{pmatrix} \quad (19)$$

where \mathbf{U} is formed by the eigenvectors of $\mathbf{A}\mathbf{A}^T$, called the left singular matrix, and \mathbf{V} is formed by the eigenvectors of $\mathbf{A}^T\mathbf{A}$, called the right singular matrix.

3.2.2 Properties of the Singular Value Decomposition Algorithm

Based on singular value decomposition theory and the matrix best approximation theorem in the sense of the Frobenius norm, it is derived that useful data information is mainly reflected by the first r larger singular values. By removing the smaller singular values that represent noise data, noise information in the original data can be effectively eliminated. Depending on the needs of the computation, not all σ_i 's have a great deal of preserved significance; therefore, smaller singular values can be omitted. The geometric significance of the data compression is shown in Fig. 2.

When using SVD to decompose a data matrix, it is very important to retain most of the important information in the matrix while minimizing the dimensionality of the decomposed matrix. In this paper, the ratio of the sum of the squares of the first r largest singular values in $\mathbf{\Sigma}$ to the sum of the squares of all the singular values is defined as the amount of information of the original data retained, as shown in (20):

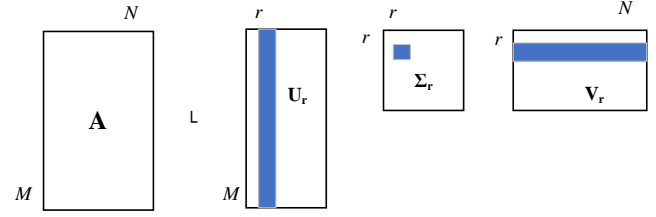


Fig. 2. Data denoising schematic.

$$\frac{\sum_{i=0}^r \lambda_i}{\sum_{i=0}^{\text{total}} \lambda_i} \geq \alpha. \quad (20)$$

A constant threshold α is usually utilized to determine the number of factors r , and then the raw data is compressed [41], [43].

3.2.3 SVD Algorithm Operation Process

If the original data set constitutes a matrix \mathbf{A} with m rows and n columns, where the rows are represented as the samples and the columns are represented as the features of the samples, then Equation (21) can be obtained by calculation:

$$\mathbf{A}^T\mathbf{A} = (\mathbf{x}^{(1)}, \mathbf{x}^{(2)}, \dots, \mathbf{x}^{(m)}) \begin{pmatrix} (\mathbf{x}^{(1)})^T \\ (\mathbf{x}^{(2)})^T \\ \vdots \\ (\mathbf{x}^{(m)})^T \end{pmatrix} \quad (21)$$

$$= \begin{pmatrix} \text{cov}(\mathbf{x}_1, \mathbf{x}_1) & \text{cov}(\mathbf{x}_1, \mathbf{x}_2) & \cdots & \text{cov}(\mathbf{x}_1, \mathbf{x}_n) \\ \text{cov}(\mathbf{x}_2, \mathbf{x}_1) & \text{cov}(\mathbf{x}_2, \mathbf{x}_2) & \cdots & \text{cov}(\mathbf{x}_2, \mathbf{x}_n) \\ \vdots & \vdots & \ddots & \vdots \\ \text{cov}(\mathbf{x}_n, \mathbf{x}_1) & \text{cov}(\mathbf{x}_n, \mathbf{x}_2) & \cdots & \text{cov}(\mathbf{x}_n, \mathbf{x}_n) \end{pmatrix}$$

where $\mathbf{x}^{(m)}$ is represented as the m -th sample, \mathbf{x}_n is represented as the n -th feature and cov is the covariance formula between the variables. Through Equation (21), it can be seen that $\mathbf{A}^T\mathbf{A}$ is the matrix describing the correlation between the features of the data set, so the orthogonal basis \mathbf{V} of $\mathbf{A}^T\mathbf{A}$ is expanded in terms of the feature space of the data set. The expansion of data set \mathbf{A} in the eigenspace is Equation (22). From the nature of singular value decomposition, the eigenvalue is represented as the information component of $\mathbf{A}^T\mathbf{A}$ in the corresponding eigenvector, and the larger the eigenvalue is, the larger the information component of the inclusion matrix $\mathbf{A}^T\mathbf{A}$ is. Therefore, the first r eigenvalues can be selected by Equation (20) to represent the original data set as shown in (23). It can be seen that the right singular matrix \mathbf{V} can be used for the compression of the matrix columns. In particular, when $r = 1$, the first principal component of the original matrix can be obtained after the matrix columns are compressed and downsized.

$$\mathbf{X}_{M \times N} = \mathbf{A}_{M \times N} \mathbf{V}_{N \times r}, \quad (22)$$

$$\mathbf{X}'_{M \times r} = \mathbf{A}_{M \times N} \mathbf{V}_{N \times r}. \quad (23)$$

Similarly, $\mathbf{A}\mathbf{A}^T$ is a matrix that describes the correlations between the sample data, so the left singular matrix \mathbf{U} is expanded in sample space, enabling row compression of the matrix.

3.3 RIME Algorithm

RIME algorithm is represented as a novel metaheuristic approach to optimization. Such algorithms often rely on the motion of objects or particles to update search agents and use the stability of objects or environments to evaluate optimal states. This, in turn, guides adjustments for subsequent iterations of the algorithm. The RIME algorithm is fundamentally inspired by natural physical laws, drawing particular inspiration from the growth mechanism of frost ice—a process where water vapor in the air directly condenses into ice crystals in low-temperature environments. The RIME algorithm is comprised of three main processes: the soft-rime formation process, the hard-rime formation process, and the positive greedy selection mechanism.

3.3.1 The Process of Soft-Rime Formation

In a breezy environment, soft-rime growth is random and soft-rime particles are free to be attached to most surfaces of an object and grow slowly in the same direction. By leveraging the strong randomness and coverage characteristics of soft rime particle growth, a soft rime particle search strategy is proposed, enabling the algorithm to search the entire search space at the beginning of each iteration and to avoid becoming trapped in local optima.

During the process of rime particles forming rime, the efficiency of particle movement is influenced by environmental factors such as temperature, humidity, and wind speed, resulting in different types of rime. At the same time, soft-rime is influenced by environmental factors and growth patterns, and will eventually stabilize rather than grow indefinitely. Consequently, based on the process of rime particles condensing to form soft-rime, Equation (24) is derived:

$$R_{ij}^{\text{new}} = R_{\text{best},j} + r_1 \cdot \cos \theta \cdot \beta \cdot (h \cdot (\text{Ub}_{ij} - \text{Lb}_{ij}) + \text{Lb}_{ij}), r_2 < E, \quad (24)$$

$$\theta = \pi \cdot \frac{t}{10 \cdot T}, \quad (25)$$

$$\beta = 1 - \frac{\left\lfloor \frac{\omega \cdot t}{T} \right\rfloor}{\omega}, \quad (26)$$

$$E = \sqrt{\frac{t}{T}} \quad (27)$$

where R_{ij}^{new} is represented as the updated position of the rime particle, i and j are represented as the i -th particle in the j -th rime-agent, respectively; parameter r_1 , r_2 are random numbers within $(-1, 1)$, and $\cos \theta$ controls the movement direction of the frost rime particle, which changes

with the number of iterations. In (25), t is the current iteration number, and T is the maximum number of iterations for the algorithm. β is represented as the environmental factor, and the change in iteration number simulates the influence of the external environment, ensuring the convergence of the algorithm. In (26) for β , β is represented as the step function, $\lfloor \cdot \rfloor$ is represented as the rounding operation, and ω has a default value of 5, which is used to control the number of segments in the step function. In (24), Ub_{ij} and Lb_{ij} are represented as the upper and lower limits of the search space, respectively, which limit the effective area for the movement of frost particles. E is the adhesion coefficient, which, along with r_2 , controls whether rime particles condense, i.e., whether the position of the rime particles is updated.

3.3.2 The Process of Hard-Rime Formation

In conditions of severe storms, there is an increased probability of frost rime puncturing the space between birth points, facilitating the exchange of rime particles. The process is beneficial for enhancing the convergence of the algorithm and the ability to escape local optima. Within the hard-rime process, the formula governing particle exchange, denoted as (28), is presented as follows:

$$R_{ij}^{\text{new}} = R_{\text{best},j}, r_3 < F^{\text{normr}}(S_i) \quad (28)$$

where R_{ij}^{new} is the new position of the updated rime particle, $R_{\text{best},j}$ is the position of the j -th particle in the best rime-agent within the rime population R . F^{normr} is represented as the normalized value of the current agent's fitness, indicating the probability of the i -th rime-agent being selected. r_3 is a random number within the interval $(-1, 1)$.

3.3.3 Positive Greedy Selection Mechanism

Greedy selection mechanisms are often employed by metaheuristic optimization algorithms. In the present algorithm, a forward greedy selection mechanism is employed for population updating, prioritizing the elimination of inefficient solutions to enhance the efficiency of global exploration. The basic principle is that the fitness values of the populations before and after the update are compared. If the fitness value improves post-update, a replacement operation is executed. This mechanism is designed to preserve existing advantages while bolstering the exploration and exploitation capabilities within the global solution space. Specifically, it not only emphasizes the optimal outcome after a single update but also, based on strategic considerations, selects and retains certain non-optimal individuals, who in turn contribute to the discovery of potentially better solutions that ultimately lead to improved global optimization results.

3.4 Extraction of Intrinsic Parameters

In this paper, the intrinsic parameters are extracted utilizing the SVD-RIME algorithm. The impact of parasitic

parameters on the intrinsic circuit model is mitigated through de-embedding techniques. The SVD algorithm is subsequently applied to the Y -parameters of the intrinsic model within the small-signal equivalent circuit model, leading to the extraction of the first principal component. Following this, a correlation analysis is conducted among the parameters to derive the fitting coefficients. By integrating these fitting coefficients with the first principal component, an optimized method for extracting the intrinsic parameters is devised. Subsequently, the RIME algorithm is employed for parameter extraction. The extraction process of the optimized intrinsic parameters is illustrated in Fig. 3.

After extracting the parasitic parameters, their influence is removed through de-embedding, and then the SVD-RIME algorithm is used to extract and optimize the intrinsic parameters. Using (29)–(32), the parameter range of the intrinsic parameters can be obtained.

$$Y_{gs} = Y_{int,11} + Y_{int,12} = \frac{j\omega C_{gs} R_{gsf}}{R_{gsf} + R_i + j\omega R_i C_{gs} R_{gsf}}, \quad (29)$$

$$Y_{gd} = -Y_{int,12} = \frac{1 + j\omega C_{gd} R_{gdf}}{R_{gdf} + R_{gd} + j\omega R_{gd} C_{gd} R_{gdf}}, \quad (30)$$

$$Y_{gm} = Y_{int,21} - Y_{int,12} = \frac{R_{gsf} G_m e^{-j\omega\tau}}{R_{gsf} + R_i + j\omega C_{gs} R_{gsf}}, \quad (31)$$

$$Y_{ds} = Y_{int,22} + Y_{int,12} = \frac{1}{R_{ds}} + j\omega C_{ds} \quad (32)$$

where $Y_{int,11}, Y_{int,12}, Y_{int,21}, Y_{int,22}$ are represented as the Y -parameters of the circuit model for the intrinsic circuit component. Y_{gs} is the gate-source admittance, Y_{gd} is the gate-drain admittance, and Y_{ds} is the drain-source admittance.

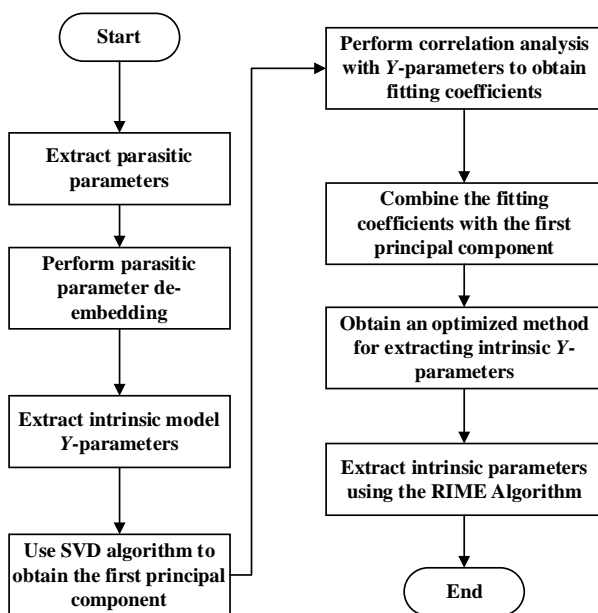


Fig. 3. Intrinsic parameter extraction process.

Then, the SVD algorithm is applied to process the Y -parameters of the intrinsic model, resulting in (33)–(34):

$$\text{Re}(Y_{int}) = \begin{bmatrix} Y_{real,11} & Y_{real,12} & Y_{real,21} & Y_{real,22} \end{bmatrix} \quad (33)$$

$$= \mathbf{U}_{real} \mathbf{W}_{real} \mathbf{V}_{real}^T,$$

$$\text{Im}(Y_{int}) = \begin{bmatrix} Y_{imag,11} & Y_{imag,12} & Y_{imag,21} & Y_{imag,22} \end{bmatrix} \quad (34)$$

$$= \mathbf{U}_{imag} \mathbf{W}_{imag} \mathbf{V}_{imag}^T,$$

$$\mathbf{V}_{real} = \begin{bmatrix} V_{real,11} & V_{real,12} & V_{real,13} & V_{real,14} \\ V_{real,21} & V_{real,22} & V_{real,23} & V_{real,24} \\ V_{real,31} & V_{real,32} & V_{real,33} & V_{real,34} \\ V_{real,41} & V_{real,42} & V_{real,43} & V_{real,44} \end{bmatrix}, \quad (35)$$

$$\mathbf{V}_{imag} = \begin{bmatrix} V_{imag,11} & V_{imag,12} & V_{imag,13} & V_{imag,14} \\ V_{imag,21} & V_{imag,22} & V_{imag,23} & V_{imag,24} \\ V_{imag,31} & V_{imag,32} & V_{imag,33} & V_{imag,34} \\ V_{imag,41} & V_{imag,42} & V_{imag,43} & V_{imag,44} \end{bmatrix} \quad (36)$$

where $\mathbf{Y}_{int} = [Y_{int,11} \ Y_{int,12} \ Y_{int,21} \ Y_{int,22}] \in \mathcal{R}^{f \times 4}$ is the parameter matrix composed of the measured values of the Y -parameters of the intrinsic model, f is the set number of frequency points. $\mathbf{U}_{real} \in \mathcal{R}^{f \times f}$ is the left singular matrix of the real part of the Y -parameter matrix of the intrinsic model; $\mathbf{W}_{real} = \text{diag}[\sigma_{real 1}, \sigma_{real 2}, \sigma_{real 3}, \sigma_{real 4}]$, $\sigma_{real 1}, \sigma_{real 2}, \sigma_{real 3}, \sigma_{real 4}$ is the singular value of the real part of the Y -parameter matrix of the intrinsic model; $\mathbf{V}_{real} \in \mathcal{R}^{4 \times 4}$ is the right singular matrix of the imaginary part of the Y -parameter matrix of the intrinsic model; $\mathbf{U}_{imag} \in \mathcal{R}^{f \times f}$ is the left singular matrix of the imaginary part of the Y -parameter matrix of the intrinsic model; $\mathbf{W}_{imag} = \text{diag}[\sigma_{imag 1}, \sigma_{imag 2}, \sigma_{imag 3}, \sigma_{imag 4}]$, $\sigma_{imag 1}, \sigma_{imag 2}, \sigma_{imag 3}, \sigma_{imag 4}$ is the singular value of the imaginary part of the Y -parameter matrix of the intrinsic model; $\mathbf{V}_{imag} \in \mathcal{R}^{4 \times 4}$ is the right singular matrix of the imaginary part of the Y -parameter matrix of the intrinsic model.

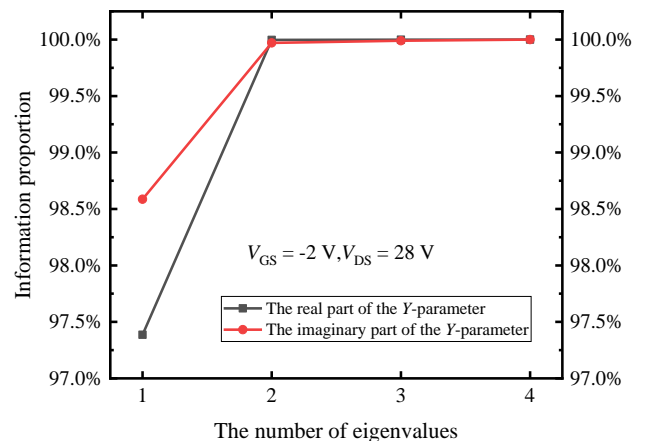


Fig. 4. Information content of singular value decomposition data.

From (20) and Fig. 4, it can be derived that the information contained in the first principal component of the Y -parameter matrix of the intrinsic model accounts for more than 90% of the total energy, so selecting the first singular value is sufficient. In this paper, column data compression is adopted for dimensionality reduction. By selecting the first singular value, i.e., extracting the first vector of matrix \mathbf{V} to form a 4×1 matrix, and then multiplying it with the original data from the right, the result, a 1-column matrix with f rows, can be obtained, thereby achieving dimensionality reduction. From (20)–(35), Equations (37), (38) can be derived:

$$F_{\text{real}} = \begin{bmatrix} Y_{\text{real},11} & Y_{\text{real},12} & Y_{\text{real},21} & Y_{\text{real},22} \end{bmatrix} \begin{bmatrix} V_{\text{real},11} \\ V_{\text{real},21} \\ V_{\text{real},31} \\ V_{\text{real},41} \end{bmatrix}, \quad (37)$$

$$F_{\text{imag}} = \begin{bmatrix} Y_{\text{imag},11} & Y_{\text{imag},12} & Y_{\text{imag},21} & Y_{\text{imag},22} \end{bmatrix} \begin{bmatrix} V_{\text{imag},11} \\ V_{\text{imag},21} \\ V_{\text{imag},31} \\ V_{\text{imag},41} \end{bmatrix}. \quad (38)$$

After performing dimensionality reduction on both the real and imaginary parts of the Y -parameters of the intrinsic model, the first principal component of the Y -parameters of the intrinsic model can be obtained, as shown in (39):

$$F_{\text{first}} = F_{\text{real}} + F_{\text{imag}}. \quad (39)$$

By conducting correlation analysis between the first principal component and each set of Y -parameters of the real and imaginary parts of the Y -parameters of the intrinsic model, the fitting coefficient for the real part is found to be a_{11} , a_{12} , a_{21} , a_{22} , and the fitting coefficient for the imaginary part is b_{11} , b_{12} , b_{21} , b_{22} . By combining these fitting coefficients with the first principal component, which is represented by (29)–(32), an optimized method for extracting the intrinsic Y -parameters is derived, as detailed in (40)–(42):

$$\text{Re}(Y_{ij}) = a_{ij} F, i, j = 1, 2, \quad (40)$$

$$\text{Im}(Y_{ij}) = b_{ij} F, i, j = 1, 2, \quad (41)$$

$$F = v_{\text{real},11} \frac{G_{\text{gsf}} + R_1 G_{\text{gsf}}^2 + \omega^2 R_1 C_{\text{gs}}^2}{(1 + R_1 G_{\text{gsf}})^2 + \omega^2 R_1^2 C_{\text{gs}}^2} + v_{\text{real},41} G_{\text{ds}} + v_{\text{real},31} \frac{(1 + R_1 G_{\text{gsf}}) G_m \cos(\omega\tau) - G_m \omega C_{\text{gs}} \sin(\omega\tau)}{(1 + R_1 G_{\text{gsf}})^2 + \omega^2 C_{\text{gs}}^2} + v_{\text{imag},11} \frac{\omega C_{\text{gs}}}{(1 + R_1 G_{\text{gsf}})^2 + \omega^2 R_1^2 C_{\text{gs}}^2} + v_{\text{imag},41} \omega C_{\text{ds}} + (v_{\text{imag},11} - v_{\text{imag},21} + v_{\text{imag},41} - v_{\text{imag},31}) \times \frac{\omega C_{\text{gd}}}{(1 + R_{\text{gd}} G_{\text{gdf}})^2 + \omega^2 R_{\text{gd}}^2 C_{\text{gd}}^2} +$$

$$+ v_{\text{real},31} \frac{-(1 + R_1 G_{\text{gsf}}) G_m \sin(\omega\tau) - \omega G_m C_{\text{gs}} \cos(\omega\tau)}{(1 + R_1 G_{\text{gsf}})^2 + \omega^2 C_{\text{gs}}^2} + (v_{\text{real},11} - v_{\text{real},21} + v_{\text{real},41} - v_{\text{real},31}) \times \frac{G_{\text{gdf}} + R_{\text{gd}} G_{\text{gdf}}^2 + \omega^2 R_{\text{gd}} C_{\text{gd}}^2}{(1 + R_{\text{gd}} G_{\text{gdf}})^2 + \omega^2 R_{\text{gd}}^2 C_{\text{gd}}^2} \quad (42)$$

where F is represented as the first principal component obtained using (29)–(32) and the SVD matrix \mathbf{v} . The specific method for extracting the intrinsic parameters is shown in (43):

$$\text{Fitness} = \sum_{i,j=1,2} \sum_{k=1}^N e_{ij} (\text{Re}(Y_{ij}^{\text{mea}}(f_k) - Y_{ij}^{\text{sim}}(f_k)) + h_{ij} (\text{Im}(Y_{ij}^{\text{mea}}(f_k) - Y_{ij}^{\text{sim}}(f_k))) \quad (43)$$

where f_k is represented as the corresponding frequency point, N is the set number of frequency points, $Y_{ij}^{\text{mea}}(f_k)$ is the Y -parameter measured at the frequency point, $Y_{ij}^{\text{sim}}(f_k)$ is the Y -parameter obtained through simulation at the frequency point, and e_{ij} and h_{ij} are weighting coefficients. Equation (43) serves as the optimized objective function used in the RIME algorithm.

Once the parameters of the intrinsic circuit model are extracted, they are substituted into the Advanced Design System (ADS) for a comprehensive comparison between simulation and test results.

4. Experimental Results and Error Analysis

The effects of the small-signal model for WIN Corporation's GaN HEMT devices were verified within the frequency range from 0.5 to 20.5 GHz. A step size of 0.2 GHz was used, and a total of 101 measurement points were obtained. Figure 5(a) shows a block diagram of S-parameter measurement system. To measure the RF performance of the GaN HEMT, a Keysight N522A Vector Network Analyzer was used. It was calibrated using the Short-Open-Load-Thru (SOLT) standard with precision on-wafer calibration standards. The DC bias voltage for the device under test (DUT) was provided by a Keysight E3631A power supply. One of the photographs of the GaN HEMT DUT is presented in Fig. 5(b). In the study, the SVD-RIME algorithm was employed to optimize the intrinsic parameters of the GaN HEMT small-signal model under different bias conditions. The experiments were conducted using ADS 2023 Update 2 and MATLAB R2022a software on a computer equipped with a 3.70 GHz AMD Ryzen 5 7500F 6-Core Processor. The data processing and algorithm extraction tasks were implemented by MATLAB software. The intrinsic parameter values obtained through Traditional Measurement (TM), RIME, and SVD-RIME under three bias conditions are listed in Tab. 2–4. In the tables, the lower and upper bounds of the

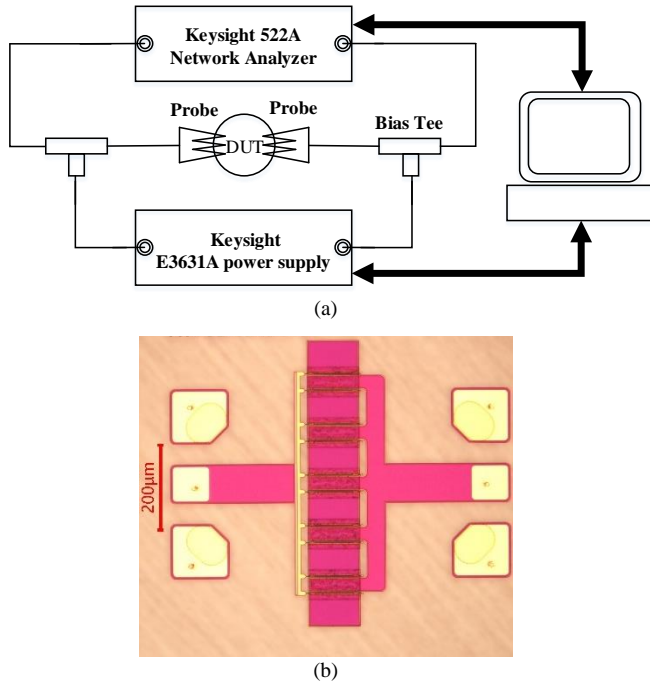


Fig. 5. (a) Block diagram of S-parameter measurement system; (b) A photograph of GaN HEMT DUT.

intrinsic parameter value range are represented by LB and UB, respectively.

After extracting the parasitic and intrinsic parameter values, these parameters were substituted into the small-signal model established in ADS to simulate the S-parameters. To gain a better understanding of the enhanced performance of the parameter extraction optimization via the SVD-RIME algorithm, comparison graphs of S-parameters between measurement and simulation results are presented in Fig. 6–8. The intrinsic parameter models extracted using the SVD-RIME algorithmic approach were shown to have better S-parameter fitting compared to the TM Method and the RIME Algorithmic Extraction Method. In particular, the small-signal circuit model obtained by the SVD-RIME algorithm in Fig. 6–8 fits the S_{21} parameters very well and is better characterized as a GaN HEMT device. Under the three bias conditions, the small-signal circuit model extracted using the SVD-RIME method is closer to the measured results.

In this paper, Equation (44), which represents the error equation, is used to conduct an error analysis of the constructed small-signal model. Based on the error calculation formula given by (44), the errors between the simulation results and the measurement results of the S-parameters of the intrinsic circuit model obtained through TM, RIME, and SVD-RIME can be derived under three different bias conditions.

$$\text{Error}_{ij} = \frac{1}{N} \sum_{k=1}^N \frac{\left| |S_{ij}^{\text{meas}}(f_k)| - |S_{ij}^{\text{model}}(f_k)| \right|}{\left| \max(S_{ij}^{\text{meas}}(f_k)) \right|}, i, j = 1, 2 \quad (44)$$

where S_{ij}^{meas} is represented as the actual measured S-parameter values, and S_{ij}^{model} is represented as the S-parameter

Elements	LB	UB	TM	RIME	SVD-RIME
C_{gd} (fF)	0	30	19.100	14.300	16.005
C_{gs} (fF)	0	650	601.100	440	470
C_{ds} (fF)	0	100	792	72	51
R_{gd} (Ω)	0	700	525.500	400	484.643
R_{gdf} (k Ω)	0	1000	295	833.931	637.565
R_i (Ω)	0	5	0.110	0.323	0.113
R_{gsf} (k Ω)	0	10	3.820	1.896	4.851
R_{ds} (Ω)	0	1000	792	762.086	642.363
G_m (S)	0	0.2	0.118	0.119	0.109
τ (ps)	0	5	2.100	2.317	0.494

Tab. 2. Values of intrinsic parameters at $V_{GS} = -2$ V, $V_{DS} = 28$ V.

Elements	LB	UB	TM	RIME	SVD-RIME
C_{gd} (fF)	0	30	21.793	18	18.593
C_{gs} (fF)	0	750	488.193	490	450
C_{ds} (fF)	0	100	40.938	60	51
R_{gd} (Ω)	0	500	332.452	290	296.953
R_{gdf} (k Ω)	0	100	45.288	47.517	60.288
R_i (Ω)	0	5	0.394	0.252	0.117
R_{gsf} (k Ω)	0	10	4.545	1.657	4.564
R_{ds} (Ω)	0	700	505	426.611	560.479
G_m (S)	0	0.5	0.119	0.113	0.108
τ (ps)	0	8	0.998	4.260	0.578

Tab. 3. Values of intrinsic parameters at $V_{GS} = -1$ V, $V_{DS} = 22$ V.

Elements	LB	UB	TM	RIME	SVD-RIME
C_{gd} (fF)	0	40	34.145	27	27.645
C_{gs} (fF)	0	650	407.500	397	367
C_{ds} (fF)	0	100	67.338	64	64
R_{gd} (Ω)	0	400	246.056	172	176.056
R_{gdf} (k Ω)	0	300	111.475	115.953	121.475
R_i (Ω)	0	5	0.127	0.211	0.103
R_{gsf} (k Ω)	0	10	5.271	1.039	4.993
R_{ds} (Ω)	0	1000	855.240	378	498.965
G_m (S)	0	0.5	0.113	0.109	0.113
τ (ps)	0	7	1.294	4.268	0.244

Tab. 4. Values of intrinsic parameters at $V_{GS} = -2$ V, $V_{DS} = 17$ V.

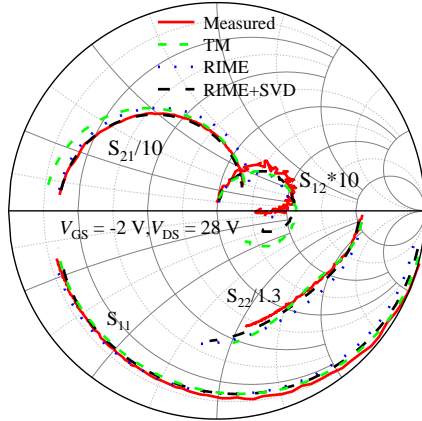


Fig. 6. S-parameter modeled results of GaN HEMT at $V_{GS} = -2\text{ V}$, $V_{DS} = 28\text{ V}$.

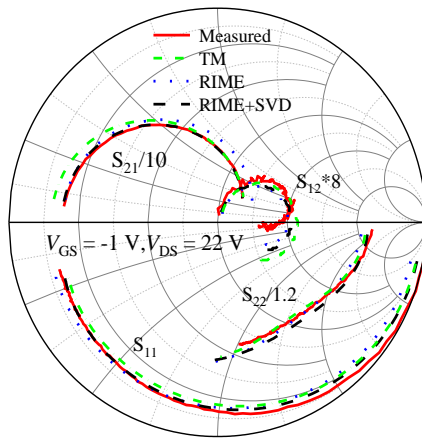


Fig. 7. S-parameter modeled results of GaN HEMT at $V_{GS} = -1\text{ V}$, $V_{DS} = 22\text{ V}$.

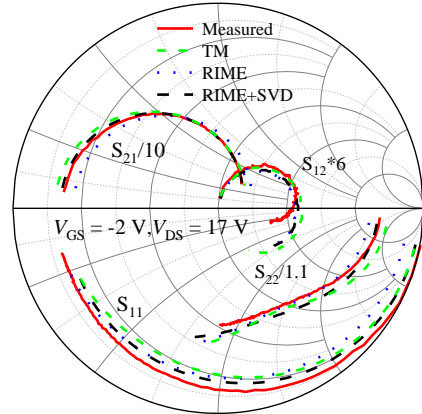


Fig. 8. S-parameter modeled results of GaN HEMT at $V_{GS} = -2\text{ V}$, $V_{DS} = 17\text{ V}$.

values obtained through simulation of the constructed small-signal model. The frequency-dependent variations in S-parameter errors for gallium nitride high electron mobility transistors are depicted in Fig. 9–11. The results of the error analysis are presented in Tab. 5. When using the RIME algorithm, the parameter extraction error is lower than that of the traditional extraction method. However, the parameter error obtained through the SVD-RIME

algorithm is even smaller, indicating better optimization results.

An in-depth comparison of the proposed SVD-RIME algorithm, the RIME algorithm, and the TM algorithm is presented in Tab. 6. Based on the comparison conducted, as well as the previously mentioned analysis of error metrics and fitting performance, it can be concluded that the SVD-RIME algorithm is superior to the other algorithms

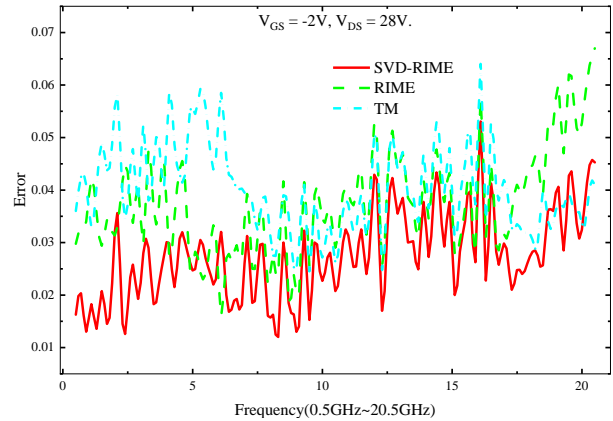


Fig. 9. Error varies with frequency for GaN HEMT at $V_{GS} = -2\text{ V}$, $V_{DS} = 28\text{ V}$.

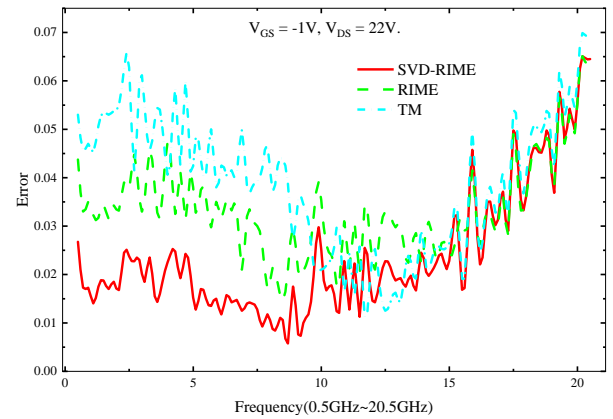


Fig. 10. Error varies with frequency for GaN HEMT at $V_{GS} = -1\text{ V}$, $V_{DS} = 22\text{ V}$.

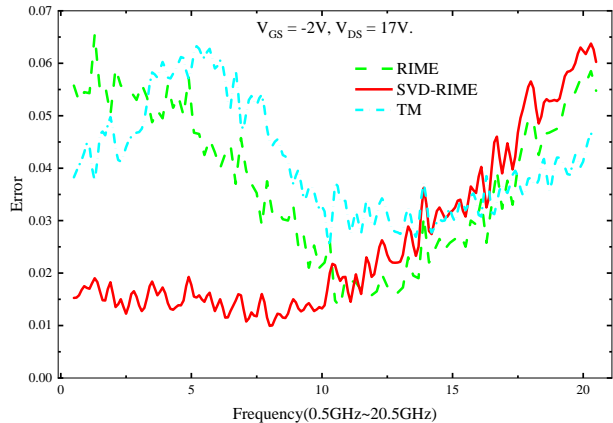


Fig. 11. Error varies with frequency for GaN HEMT at $V_{GS} = -2\text{ V}$, $V_{DS} = 17\text{ V}$.

Bias point	Algorithm	S ₁₁ (dB)	S ₁₂ (dB)	S ₂₁ (dB)	S ₂₂ (dB)	Error _{avg}
V _{GS} = -2 V V _{DS} = 28 V	TM	2.8%	5.6%	3.6%	4.2%	4.0%
	Rime	1.6%	5.9%	3.0%	4.5%	3.7%
	SVD-Rime	1.5%	4.0%	2.1%	3.4%	2.7%
V _{GS} = -1 V V _{DS} = 22 V	TM	2.9%	7.4%	1.2%	4.1%	3.9%
	Rime	2.7%	4.2%	1.2%	5.3%	3.3%
	SVD-Rime	1.0%	3.8%	1.0%	3.8%	2.4%
V _{GS} = -2 V V _{DS} = 17 V	TM	5.4%	4.9%	1.7%	3.5%	4.1%
	Rime	3.3%	3.6%	3.0%	5.1%	3.8%
	SVD-Rime	3.0%	3.4%	0.5%	3.5%	2.6%

Tab. 5. GaN HEMT S-parameter error results.

Algorithm	Implementation Complexity	Computational Efficiency	Accuracy	Robustness
TM	Low	High	Moderate	Poor
Rime	Medium	Medium	High	Moderate
SVD-Rime	High	Medium	Highest	Strongest

Tab. 6. A comprehensive comparison table.

5. Conclusion

In order to accurately describe the small-signal characteristics of GaN HEMTs, the SVD-RIME algorithm is introduced and applied in this paper to optimize and extract their intrinsic parameters. The SVD algorithm is used as a powerful data processing technique for data compression and reconstruction. By retaining the basic information characteristics of the data and correlating them with the Y -parameters, the proposed intrinsic model Y -parameter extraction method breaks the isolation between various intrinsic parameters, leading to an improvement in the accuracy of intrinsic parameter extraction. The SVD-RIME algorithm is shown to be remarkably efficacious in extracting and optimizing the intrinsic parameters of small-signal circuit models as compared to conventional extraction methods and those based on the RIME algorithm. The experimental results show that the small-signal equivalent circuit model can be derived by extracting the intrinsic model parameters using the SVD-RIME algorithm within the frequency range of 0.5 GHz to 20.5 GHz. The parametric simulation results are in good agreement with the measurement results. Therefore, the accuracy and validity of the SVD-RIME method are confirmed.

Acknowledgments

This work was supported by Henan Province Higher Education Young Backbone Teachers Training Program (Grant No. 2023GGJS045) and Henan Provincial Science & Technology Research Project of China (Grant No. 242102211103).

References

- [1] ISLAM, N., MOHAMED, M. F. P., KHAN, M. F. A. J., et al. Reliability, applications and challenges of GaN HEMT technology for modern power devices: A review. *Crystals*, 2022, vol. 12, no. 11, p. 1–42. DOI: 10.3390/cryst12111581
- [2] PECHEUX, R., KABOUCHE, R., DOGMUS, E., et al. Importance of buffer configuration in GaN HEMTs for high microwave performance and robustness. In *2017 47th European Solid-State Device Research Conference (ESSDERC)*. Leuven (Belgium), 2017, p. 228–231. DOI: 10.1109/ESSDERC.2017.8066633
- [3] HUSNA HAMZA, K., NIRMAL, D. A review of GaN HEMT broadband power amplifiers. *AEU - International Journal of Electronics and Communications*, 2020, vol. 116, p. 1–11. DOI: 10.1016/j.aeu.2019.153040
- [4] LUONG, D. M., TRAN, X. N. An independently biased 3-stacked GaN HEMT power amplifier for next-generation wireless communication systems. *Radioengineering*, 2020, vol. 29, no. 4, p. 617–624. DOI: 10.13164/re.2020.0617
- [5] LIU, R., MEI, B., SU, Y., et al. The effects and mechanisms of 2 MeV proton irradiation on high bias conditions of InP/InGaAs DHBTs. *Solid-State Electronics*, 2024, vol. 212, p. 1–6. DOI: 10.1016/j.sse.2023.108832
- [6] ZHANG, J., MEI, B., SU, Y., et al. Influence of BCB protection on irradiation response of InP-based HEMTs: A comparative study. *IEEE Transactions on Electron Devices*, 2023, vol. 70, no. 8, p. 4225–4230. DOI: 10.1109/TED.2023.3287816
- [7] ZHANG, C., SU, Y., MEI, B., et al. Effect of proton irradiation on interfacial and electrical performance of N+Np+ InP/InGaAs hetero-junction. *Current Applied Physics*, 2023, vol. 48, p. 47–52. DOI: 10.1016/j.cap.2023.01.013
- [8] KOTECHA, R. M., ZHANG, Y., RASHID, A., et al. A physics-based compact device model for GaN HEMT power devices. In *2016 IEEE 4th Workshop on Wide Bandgap Power Devices and Applications (WiPDA)*. Fayetteville (AR, USA), 2016, p. 108–113. DOI: 10.1109/WiPDA.2016.7799919

- [9] HUSAIN, S., HASHMI, M., GHANNOUCHI, F. M. Comprehensive investigation and comparative analysis of machine learning-based small-signal modelling techniques for GaN HEMTs. *IEEE Journal of the Electron Devices Society*, 2022, vol. 10, p. 1015–1032. DOI: 10.1109/JEDS.2022.3224433
- [10] HUSAIN, S., JARNDAL, A., HASHMI, M., et al. Accurate, efficient and reliable small-signal modeling approaches for GaN HEMTs. *IEEE Access*, 2023, vol. 11, p. 106833–106846. DOI: 10.1109/ACCESS.2023.3317530
- [11] ZHU, G., CHANG, C., XU, Y., et al. A millimeter-wave scalable small-signal modeling approach based on FW-EM for AlGaIn/GaN HEMT up to 110 GHz. *Microwave and Optical Technology Letters*, 2021, vol. 63, no. 8, p. 2145–2152. DOI: 10.1002/mop.32404
- [12] TANG, X., YANG, T., JIA, Y., et al. FW-EM-based approach for scalable small-signal modeling of GaN HEMT with consideration of temperature-dependent resistances. *International Journal of Numerical Modelling: Electronic Networks, Devices and Fields*, 2021, vol. 34, no. 5, p. 1–10. DOI: 10.1002/jnm.2882
- [13] ISSAOUN, A., ROEDLE, T. Simple small-signal HEMT model suitable for GaN stability analysis and technologies benchmarking. *Journal of Applied Physics*, 2021, vol. 6, no. 1, p. 1–8. DOI: 10.11648/j.wjap.20210601.11
- [14] AAMIR AHSAN, S., PAMPORI, A.-H., GHOSH, S., et al. A new small-signal parameter extraction technique for large gate-periphery GaN HEMTs. *IEEE Microwave and Wireless Components Letters*, 2017, vol. 27, no. 10, p. 918–920. DOI: 10.1109/LMWC.2017.2746661
- [15] CHEN, Y., XU, Y., LUO, Y., et al. A reliable and efficient small-signal parameter extraction method for GaN HEMTs. *International Journal of Numerical Modelling: Electronic Networks, Devices and Fields*, 2020, vol. 33, no. 3, p. 1–14. DOI: 10.1002/jnm.2540
- [16] CHIGAEVA, E., WALTHES, W., WIEGNER, D., et al. Determination of small-signal parameters of GaN-based HEMTs. In *Proceedings 2000 IEEE/Cornell Conference on High Performance Devices (Cat. No.00CH37122)*. Ithaca (NY, USA), 2000, p. 115–122. DOI: 10.1109/CORNEL.2000.902526
- [17] KHUSRO, A., HUSAIN, S., HASHMI, M. S., et al. A generic and efficient globalized kernel mapping-based small-signal behavioral modeling for GaN HEMT. *IEEE Access*, 2020, vol. 8, p. 195046 to 195061. DOI: 10.1109/ACCESS.2020.3033788
- [18] COLANGELI, S., CICCIGNANI, W., CLERITI, R., et al. Optimization-based approach for scalable small-signal and noise model extraction of GaN-on-SiC HEMTs. *International Journal of Numerical Modelling: Electronic Networks, Devices and Fields*, 2017, vol. 30, no. 1, p. 1–16. DOI: 10.1002/jnm.2135
- [19] HUSSEIN, A. S., JARNDAL, A. H. Reliable particle-swarm-optimization based parameter extraction method applied to GaN HEMTs. In *2016 16th Mediterranean Microwave Symposium (MMS)*. Abu Dhabi (United Arab Emirates), 2016, p. 1–4. DOI: 10.1109/MMS.2016.7803850
- [20] ABUSHAWISH, A., JARNDAL, A. Comparison of GA, GWO, and HHO optimization techniques for modeling substrate/buffer loading effect on GaN HEMTs. In *2021 14th International Conference on Developments in eSystems Engineering (DeSE)*. Sharjah (United Arab Emirates), 2021, p. 376–381. DOI: 10.1109/DeSE54285.2021.9719328
- [21] ZHANG, J., HOU, X., LIU, M., et al. Hybrid small-signal modeling of GaN HEMTs based on improved genetic algorithm. *Microelectronics Journal*, 2022, vol. 127, p. 1–9. DOI: 10.1016/j.mejo.2022.105513
- [22] WANG, S., ZHANG, J., YANG, S., et al. Hybrid small-signal model parameter extraction for GaN HEMT based on QGA. *International Journal of Electronics*, 2023, vol. 111, no. 4, p. 729 to 747. DOI: 10.1080/00207217.2023.2188610
- [23] HUANG, F. Y., TANG, X. S., WEI, Z. N., et al. An improved small-signal equivalent circuit for GaN high-electron mobility transistors. *IEEE Electron Device Letters*, 2016, vol. 37, no. 11, p. 1399–1402. DOI: 10.1109/LED.2016.2609462
- [24] CRUPI, G., CADDEMI, A., SCHREURS, D. M. M.-P., et al. The large world of FET small-signal equivalent circuits (invited paper): FET small-signal equivalent circuits. *International Journal of RF and Microwave Computer Aided Engineering*, 2016, vol. 26, no. 9, p. 749–762. DOI: 10.1002/mmce.21028
- [25] WEISER, M. C. J., HÜCKELHEIM, J., KALLFASS, I. A Novel approach for the modeling of the dynamic ON-State resistance of GaN-HEMTs. *IEEE Transactions on Electron Devices*, 2021, vol. 68, no. 9, p. 4302–4309. DOI: 10.1109/TED.2021.3098498
- [26] CRUPI, G., SCHREURS, D. M. M.-P., CADDEMI, A., et al. High-frequency extraction of the extrinsic capacitances for GaN HEMT technology. *IEEE Microwave and Wireless Components Letters*, 2011, vol. 21, no. 8, p. 445–447. DOI: 10.1109/LMWC.2011.2160525
- [27] JARNDAL, A., CRUPI, G., ALIM, M. A., et al. Equivalent-circuit extraction for gallium nitride electron devices: Direct versus optimization-empowered approaches. *International Journal of Numerical Modelling: Electronic Networks, Devices and Fields*, 2022, vol. 35, no. 5, p. 1–11. DOI: 10.1002/jnm.3008
- [28] SU, H., ZHAO, D., HEIDARI, A. A., et al. RIME: A physics-based optimization. *Neurocomputing*, 2023, vol. 532, p. 183–214. DOI: 10.1016/j.neucom.2023.02.010
- [29] ZHONG, R., YU, J., ZHANG, C., et al. SRIME: A strengthened RIME with Latin hypercube sampling and embedded distance-based selection for engineering optimization problems. *Neural Computing and Applications*, 2024, vol. 36, no. 12, p. 6721–6740. DOI: 10.1007/s00521-024-09424-4
- [30] HÖCKER, A., KARTVELISHVILI, V. SVD approach to data unfolding. *Nuclear Instruments and Methods in Physics Research Section A: Accelerators, Spectrometers, Detectors and Associated Equipment*, 1996, vol. 372, no. 3, p. 469–481. DOI: 10.1016/0168-9002(95)01478-0
- [31] RUBINSTEIN, R., PELEG, T., ELAD, M. Analysis K-SVD: A dictionary-learning algorithm for the analysis sparse model. *IEEE Transactions on Signal Processing*, 2013, vol. 61, no. 3, p. 661–677. DOI: 10.1109/TSP.2012.2226445
- [32] ANDREWS, H., PATTERSON, C. Singular Value Decomposition (SVD) image coding. *IEEE Transactions on Communications*, 1976, vol. 24, no. 4, p. 425–432. DOI: 10.1109/TCOM.1976.1093309
- [33] ZHU, W., LI, Z., HEIDARI, A. A., et al. An enhanced RIME optimizer with horizontal and vertical crossover for discriminating microseismic and blasting signals in deep mines. *Sensors*, 2023, vol. 23, no. 21, p. 1–33. DOI: 10.3390/s23218787
- [34] LI, Y., ZHAO, D., MA, C., et al. CDRIME-MTIS: An enhanced rime optimization-driven multi-threshold segmentation for COVID-19 X-ray images. *Computers in Biology and Medicine*, 2024, vol. 169, p. 1–56. DOI: 10.1016/j.combiomed.2023.107838
- [35] ZHU, W., FANG, L., YE, X., et al. IDRIM: Brain tumor image segmentation with boosted RIME optimization. *Computers in Biology and Medicine*, 2023, vol. 166, p. 1–18. DOI: 10.1016/j.combiomed.2023.107551
- [36] OOI, B. L., MA, J. Y. Consistent and reliable MESFET parasitic capacitance extraction method. *IEE Proceedings - Microwaves, Antennas and Propagation*, 2004, vol. 151, no. 1, p. 81–84. DOI: 10.1049/ip-map:20040128

- [37] ZHANG, J., WANG, S., LIU, M., et al. An improved GaN P-HEMT small-signal equivalent circuit with its parameter extraction. *Microelectronics Journal*, 2021, vol. 112, p. 1–6. DOI: 10.1016/j.mejo.2021.105042
- [38] KHUSRO, A., HASHMI, M. S., ANSARI, A. Q., et al. An accurate and simplified small signal parameter extraction method for GaN HEMT. *International Journal of Circuit Theory and Applications*, 2019, vol. 47, no. 6, p. 941–953. DOI: 10.1002/cta.2622
- [39] CHEN, G., KUMAR, V., SCHWINDT, R. S., et al. A low gate bias model extraction technique for AlGaIn/GaN HEMTs. *IEEE Transactions on Microwave Theory and Techniques*, 2006, vol. 54, no. 7, p. 2949–2953. DOI: 10.1109/TMTT.2006.877047
- [40] MAJUMDAR, S., BAG, A., BISWAS, D. Comparative analysis of parameter extraction techniques for AlGaIn/GaN HEMT on silicon/sapphire substrate. *Microelectronics Reliability*, 2017, vol. 78, p. 389–395. DOI: 10.1016/j.microrel.2017.08.016
- [41] ZHANG, Z. The singular value decomposition, applications and beyond. Oct. 29, 2015. *arXiv*: arXiv:1510.08532, p. 1–114. DOI: 10.48550/arXiv.1510.08532
- [42] MEES, A. I., RAPP, P. E., JENNINGS, L. S. Singular-value decomposition and embedding dimension. *Physical Review A*, 1987, vol. 36, no. 1, p. 340–346. DOI: 10.1103/PhysRevA.36.340
- [43] DEMIREL, H. ANBARJAFARI, G. JAHROMI, M. N. S. Image equalization based on singular value decomposition. In *2008 23rd International Symposium on Computer and Information Sciences*. Istanbul (Turkey), 2008, p. 1–5. DOI: 10.1109/ISCIS.2008.4717878

About the Authors ...

Jincan ZHANG was born in Xingtai, China, in 1985. He received the M.S. degree in Xi'an University of Technology, Xi'an, China, in 2010. He received the Ph.D. degree in XiDian University, Xi'an, China, in June 2014. Now he is an Associate Professor in Henan University of Science and Technology, Luoyang, China. His research is focused on modeling of HBTs and design of very high speed integrated circuits.

Kexin WANG was born in 2000 in Kaifeng, China. She received the Bachelor's degree from Henan University of Science and Technology in 2024. She is currently pursuing her master's degree at Henan University of Science and Technology. Her research is focused on modeling of GaN HEMT device.

Jinchan WANG was born in Luoyang, China, in 1980. She received the Ph.D. degree in the Southeast University, Nanjing, China, in June 2009. Now she is an Associate Professor in Henan University of Science and Technology, Luoyang, China. Her research is focused on semiconductor materials and devices.

Haobo WEI was born in Zhengzhou, China, in 2002. He is currently pursuing his bachelor's degree at Henan University of Science and Technology, specializing in electronic science and technology.

Jingyu CHANG was born in 2001. He obtained his B.Eng. degree from Henan University of Science and Technology, Luoyang, from 2020 to 2024. His research is focused on modeling of GaN HEMT and design of very high speed integrated circuit.

Jiahao YAO was born in 2001. He obtained his B.E. degree in Engineering from Zhengzhou University of Aeronautics, Zhengzhou, from 2020 to 2024; and is currently pursuing his M.S. degree in Engineering at Henan University of Science and Technology. His major field is modeling and simulation of semiconductor devices.

Liwen ZHANG was born in 1980. She obtained her B.E and M.S. degree in Physics from Zhengzhou University, Zhengzhou, from 1997 to 2004; then received her Ph.D. degree in Atomic and Molecular Physics at Wuhan Institute of Physics and Mathematics, Chinese Academy of Sciences, Wuhan, in 2008. She is currently a Professor in Henan University of Science and Technology. Her major field is modeling and simulation in advanced packaging development.